ELEVENTH INTERNATIONAL CONFERENCE ON INTERGRANULAR AND INTERPHASE BOUNDARIES 2004

JOURNAL OF MATERIALS SCIENCE **40** (2005) 3081–3090

Titanium-oxide interface structures formed by degassing and anodization processes

Y. TANAKA
Division of Dental and Biomedical Materials Science, Department of Developmental and Reconstructive Medicine, Course of Medical and Dental Sciences, Graduate School of Biomedical Sciences, Nagasaki University, 1-7-1 Sakamoto, Nagasaki 852-8588, Japan
E-mail: y-tanaka@net.nagasaki-u.ac.jp

High-resolution electron microscopy was used to investigate two types of titanium-oxide interface structures. The first type was generated by thermal oxidation during the degassing process, which is one step in the process of porcelain-fused-to-metal systems. The thermal oxidation was performed for 1 min at a temperature of 1073 K in a porcelain furnace under a reduced pressure at 27 hPa. Columnar and granular rutile oxide formed on the titanium, and the surface oxide layer was almost 1 μm thick. On an atomic scale, the crystal size of the rutile adjacent to the interface decreased about 10 nm. In addition, a very thin transitional layer 2–3 nm thick formed at the titanium-oxide interface. The crystal structure of the thin layer seemed to be the TiO phase with a NaCl-type structure. The interface between the hcp titanium and TiO phases was coherent through the close-packed planes $((0\ 0\ 0\ 2)_{hcp}$ and $(1\ 1\ 1)_{TiO})$. Partial coherency was observed at the interface between the TiO and TiO_2 phases. The second type of titanium-oxide interface was generated by anodization on a screw-type titanium implant. The morphology of the surface suggested that the titanium implant had been treated by spark anodization. The surface oxide, which was estimated to be about 10 μm thick, was a mixture of the anatase-type TiO_2 phase and the amorphous phase. The crystal size of the anatase varied from less than 10 nm to more than 100 nm. A phosphate anion was concentrated in the amorphous phase. Between the surface oxide and the titanium base, macroscopic defects like cracks and voids were observed. Microscopic observation could not confirm the formation of a clear interface and lattice coherency between the titanium and oxide as a result of the degassing process.
© *2005 Springer Science + Business Media, Inc.*

1. Introduction

Titanium is one of the most promising dental materials for the future. Indeed, the number of applications of titanium is steadily growing, for example, in prostheses made by dental precise casting systems [1], in implants due to its excellent biocompatibility [2], and in superelastic Ni-Ti orthodontic wires [3].

One problem of titanium crowns or bridges is the lack of aesthetics because of the metallic color of titanium. To imitate tooth color, a porcelain-fused-to-metal (PFM) technique was developed for dental metal restorations [4, 5]. The PFM technique has been evolving since the 1960's for dental gold alloys, including establishing a lower fusing temperature for porcelain than the melting temperature of the gold alloy, making fine adjustments of the thermal expansion coefficients between the metal and the porcelain, adding base metal elements to the gold alloy to enhance the bond strength between the porcelain and metal, and roughening the metal surface by sandblasting to obtain improved bonding strength by the anchor effect.

Likewise, veneering tooth-colored porcelain on titanium achieves favorable aesthetics. The first attempt to apply the PFM technique to titanium was performed in the 1980's [6]. In the next decade, a commercial PFM system was created for titanium, although the bond strength between titanium and porcelain was lower than between gold alloy and porcelain [7–9]. Several problems remain to be solved regarding the bonding of porcelain to titanium.

Degassing is one step in the PFM process. If gas remains on the metal surface, a void that could initiate a crack will form at the metal-porcelain interface when the porcelain is fused. During the degassing process, the metal is subjected to high temperatures near the fusing temperature. A clean surface is created by burning off any organic matter, and the metal surface is oxidized. Nowadays, the main purpose of degassing is oxidation, since the oxide is considered to behave like an intermediary between the metal and porcelain [4, 10].

Most structural investigations of PFM interfaces have been performed using a scanning electron microscope (SEM) [11–16] and an electron spectroscopy for chemical analysis (ESCA) system [17–19]. In order to appraise the contribution of the chemical bond in the interface, however, it is necessary to observe the interface

on an atomic scale because the spatial range of the chemical interaction is at an atomic level. Therefore, we studied the nanostructure of the PFM interface using transmission electron microscopy (TEM). Because we found an interesting structure on the titanium-oxide interface after the degassing process, the first subject addressed in this paper will be the titanium-oxide interface formed during degassing.

Oxidation due to degassing takes place in a dry environment, while oxidation created by anodization occurs in a wet environment. In some titanium implants, the surfaces are modified to improve the biocompatibility; anodization is one of these techniques [20]. To enhance osseointegration, anodized titanium implants are now commercially available. The functional performance derived from surface modification should be closely related to the surface microstructure and chemical state. In particular, if an anatase-type oxide is formed, many functions like photocatalysis, disinfection and hydrophilication are expected [21, 22]. Therefore, we also used TEM to investigate the nanostructure of anodized titanium and found that the structure of the anodized titanium was different from that of the degassed titanium. In the second part of this paper, the cross-sectional structure of anodized titanium implants will be discussed.

2. Materials and methods

2.1. Degassed titanium (thermal oxidation)

Grade II commercially pure titanium (CP Ti) (JIS H 4650 type 2, 99.5% purity) was used in this study. Cylindrical specimens (ϕ2.5 mm $\times$ 7 mm) were cast into a mold with MgO-based investment (Selevest CB, Selec, Japan) using an argon arc-melting, centrifugal dental titanium casting machine (Ticast Super R, Selec). Each specimen was cut into semicylinders with a low speed saw (Isomet, Buehler). The cut surface was polished with #1500 abrasive paper and a polishing cloth to obtain a flat surface.

The degassing process followed the manufacturer's instructions. The titanium specimens were heat-treated in a commercial porcelain furnace (Commodore 75/VPF, Jelenko) from 823 to 1073 K at a heating rate of 50 K/min and held 60 s in a vacuum of 27 hPa. After treatment, the specimens were air-cooled.

The specimens were prepared for TEM observation as follows. Two pieces of degassed specimens were glued into a Cu pipe with an epoxy adhesive (G-1 epoxy, Gatan). The disk specimens were cut using the low speed saw and mechanically ground down to a thickness of 50 μm. The center of the disk specimen was then dimpled to 20 μm thickness with a dimple grinder (Model 656, Gatan). Finally, the cross-sectional TEM specimens were thinned using precise ion polishing equipment (PIPS-691, Gatan). The specimens were irradiated using an argon ion beam with an accelerating voltage of 4 kV from a low incident angle of 4°.

2.2. Anodized titanium implant

A commercial screw-type implant made of commercially pure (CP) titanium (TiUnite^{TM} , Nobel Biocare) was examined. To ensure biocompatibility, the surface of the screw section, which is implanted in the jaw, was modified by anodization. As a result, the surface morphology was rough, making it impossible to prepare cross-sectional TEM specimens without a focused ion beam apparatus (FIB).

The thinning process for preparing the TEM specimens was as follows. The threaded screw portion of the implant was cut in round slices, and each sliced specimen was mechanically ground down to 50 μm thickness using abrasive papers. Then the specimen was divided into sector pieces. Finally, the cross-sectional TEM specimen was thinned using an FIB (Hitachi FB-2000 K) and irradiated with a Ga ion beam at an accelerating voltage of 30 kV.

2.3. TEM observations

TEM observation was performed using a 200 kV TEM (JEOL JEM-2010 HT). Selected area diffraction (SAD) patterns were produced from an area of about 100 nm in diameter. Chemical analysis was carried out using energy dispersive X-ray (EDX) spectroscopy with a 15 nm electron beam probe.

3. Results and discussion

3.1. Thermal oxidation

Fig. 1a shows a low-magnification TEM image of a specimen cross section after the degassing process. The TEM specimens were fabricated by gluing two pieces of titanium half-cylinders, so that surface oxide layers face each other. A thickness of the surface oxide layer is quite uniform and several hundred nm. Somewhat larger number of dislocations can be seen in the titanium. An enlarged micrograph of the surface oxide (Fig. 1b) shows that large columnar oxide crystals have grown toward the surface. Small, round crystal grains of about 100 nm are located beneath the columnar crystals. Between the small crystals and titanium, a very fine contrast of about 10 to 20 nm is visible.

We examined the structure of each type of oxide crystal. TEM micrographs and corresponding diffraction patterns of the columnar crystals [labelled "A" in Fig. 1a] and the small crystals ("B" in Fig. 1a) are shown

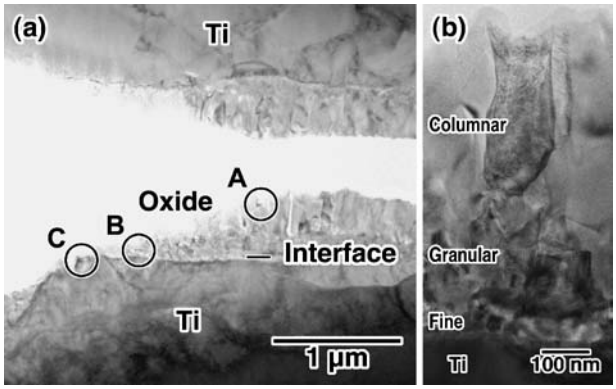

Figure 1 Cross-sectional TEM micrographs of the titanium-oxide interface after the degassing process. (a) A low-magnification image, (b) An enlarged image of the surface oxide layer.

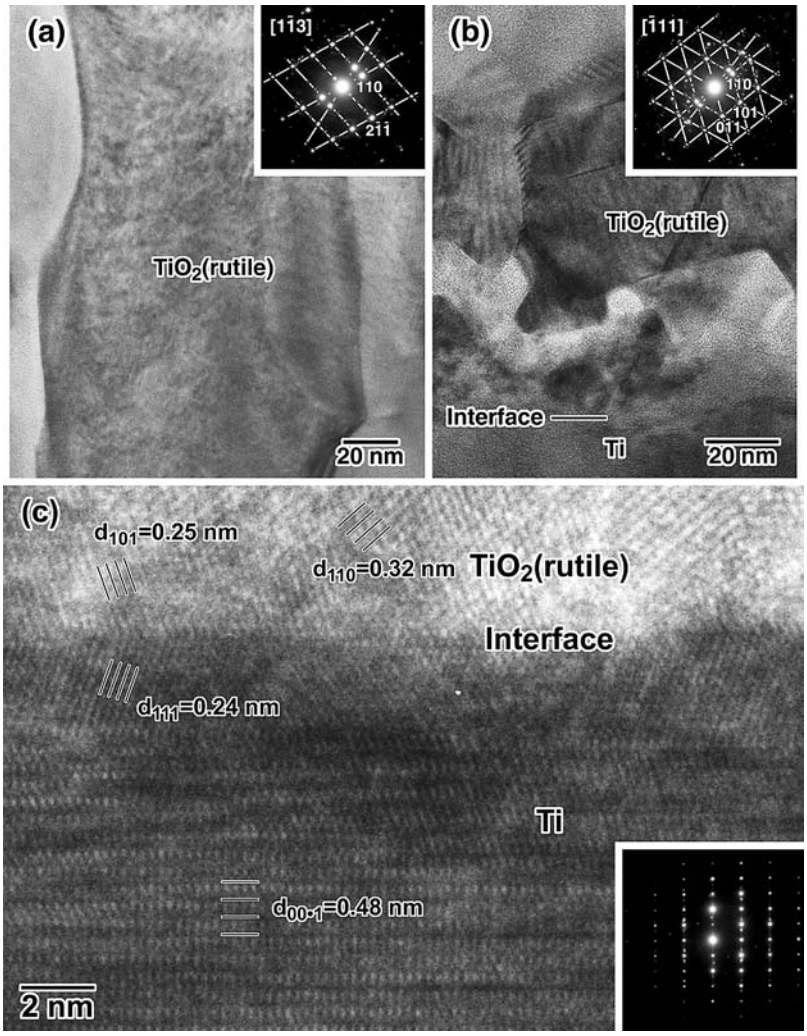

Figure 2 TEM micrographs and diffraction patterns (inset) of (a) columnar and (b) granular oxide crystals taken from points "A" and "B" in Fig. 1a, respectively. (c) HRTEM micrograph and diffraction pattern (inset) of the titanium-oxide interface taken from point "C" in Fig. 1a.

in Fig. 2a and b, respectively. The SAD patterns revealed that both the oxides consist of TiO_2 phase with a rutile structure. In Fig. 2b, fine, mottled-looking crystallites (less than 10 nm) are found adjacent to the titanium. A high-resolution TEM (HRTEM) image of the interface between the titanium and the oxide ("C" in Fig. 1a) is shown in Fig. 2c, with the corresponding SAD pattern in the inset of Fig. 2c. The upper half of the micrograph shows that the crystallites (about 10 nm in size) are the rutile phase since the plane spacing corresponds to the value for the rutile-type TiO_2 phase. The lower half of Fig. 2c consists of hexagonal titanium, and the incident electron beam direction is [2 $\bar{1}$ $\bar{1}$ 0]. The *c*-axial direction of the hexagonal structure is longitudinal, and a stack of (0 0 0 1) planes spaced 0.48 nm apart is seen. The flat interface between the titanium and the rutile appears parallel to the (0 0 0 1) plane. At the interface, the lattice fringe of the (0 0 0 1) plane vanishes in the thickness of 3 nm. In this part, the fcc lattice formed and has a $(1\ 1\ 1)_{fcc}//(0\ 0\ 0\ 2)_{hcp}$ relationship with the hexagonal titanium.

Some additional spots appeared in the SAD pattern [inset of Fig. 2c], which can be identified (Fig. 3) as the [2 $\bar{1}$ $\bar{1}$ 0] incident pattern of the hcp phase (white lines) and the [1 $\bar{1}$ 0] incident pattern of the fcc phase (gray lines). It is clear that the position of the 0 0 0 2 reflection spot coincides with the 1 1 1 reflection spot. The lattice parameter of the fcc phase was evaluated from the SAD pattern as $a = 0.42$ nm, and is in good agreement with $a_{calc} = 0.416$ nm, which was calculated on the assumption that the atomic radius of the fcc titanium is the same as that of the hcp titanium. The existence of the fcc titanium has been reported in the layers composed of Ti and Al [23, 24]. On the other hand, Andersson *et al*. have reported that the lattice parameter of the TiO phase with a NaCl-type structure is $a = 0.418$ nm [25]. However, it is impossible to distinguish between the fcc and NaCl structures from the conventional SAD pattern. To distinguish between fcc and NaCl structures, a dynamical method like a convergent beam electron diffraction (CBED) method must be required. However, the modified nano-layer is too thin to perform such a delicate observation for us. We considered that the modified nano-layer seems to be the NaCl structure of the TiO phase and not the fcc structure of titanium, inasmuch as the structural change took place within the narrow area adjacent to the oxide. But we could not obtain clear evidence, so we need to determine the definitive structure of the nano-layer for further investigation using, for example, a CBED method.

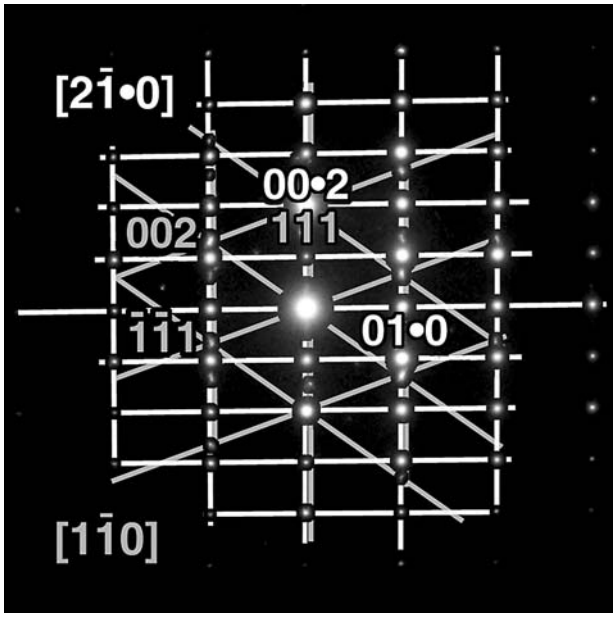

Figure 3 The same diffraction pattern in inset of Fig. 2c. The white and gray meshes indicate a diffraction pattern formed by the hcp and fcc (NaCl) structures, respectively.

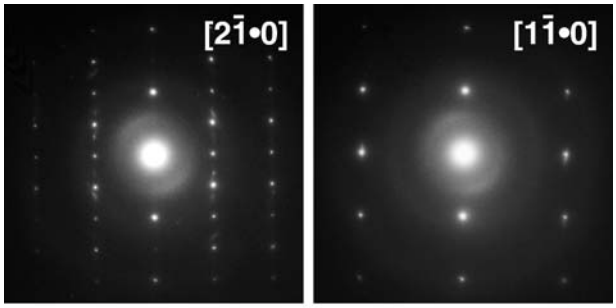

(a) 200 nm depth from Ti/oxide interface
c/*a*=1.620

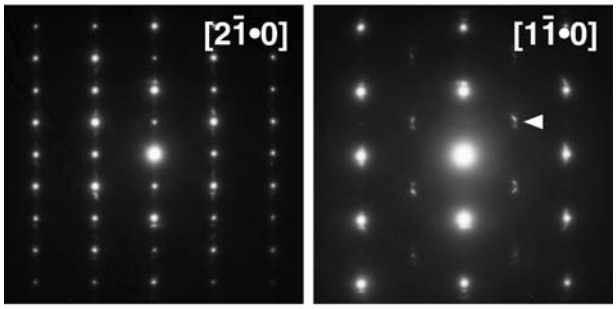

(b) 5 μm depth from Ti surface
c/*a*=1.598

Figure 4 (a), (b) Diffraction patterns taken from a depth of 200 nm (a) from the titanium-oxide interface and a depth of 5 μm (b) from the original surface.

The lattice parameters of the hcp phase evaluated from the SAD pattern in Fig. 3 are $a = 0.297$ nm, $c = 0.482$ nm and $c/a = 1.63$. For pure titanium, it is known that the axial ratio, c/a, equals 1.587 [26] and increases as the interstitial oxygen content increases. In addition, it is anticipated that a Ti_2O phase with oxygen-ordering structure will be present [25]. With respect to this Ti_2O phase, oxygen occupied the octahedral interstitial site in every (0 0 0 1) plane of the hexagonal titanium, that is, the Ti_2O phase had an anti-CdI_2-type structure. The axial ratio of the Ti_2O phase is reported to be $c/a = 1.637$. Judging from the estimated axial ratio of the SAD pattern in Fig. 3, it is possible that the Ti_2O ordered phase formed on the titanium side, since the axial ratio is close to the value of the Ti_2O phase, and the 0 0 0 1 forbidden reflection for the hcp phase appeared. However, the 0 0 0 1 forbidden reflection of the hcp phase can be made due to a double reflection under the condition of the [2 $\bar{1}$ $\bar{1}$ 0] incident electron beam direction.

In the [1 $\bar{1}$ 0 0] incident electron beam direction, the generation of the 0 0 0 1 double diffraction is suppressed. Figs 4a and b show the SAD patterns of the [2 $\bar{1}$ $\bar{1}$ 0] and [1 $\bar{1}$ 0 0] incident electron beam directions taken from a depth of 200 nm from the interface and 5 μm from the surface, respectively. In the diffraction pattern taken near the interface (Fig. 4a), the 0 0 0 1 forbidden reflection disappeared although the axial ratio was determined to be $c/a = 1.620$. The disappearance in the [2 $\bar{1}$ $\bar{1}$ 0] incident electron beam direction depended on slight changes in the direction the goniometer was tilted. In contrast, the 0 0 0 1 forbidden reflection emerged in the [2 $\bar{1}$ $\bar{1}$ 0] diffraction pattern (Fig. 4b) although the axial ratio measured inside the titanium was $c/a = 1.598$, which was closer to the value of pure titanium. In either case, the 0 0 0 1 forbidden reflection disappeared under the [1 $\bar{1}$ 0 0] incident electron beam condition. Consequently, the 0 0 0 1 forbidden reflection observed under the [2 $\bar{1}$ $\bar{1}$ 0] incident condition was not caused by the ordering arrangement of the interstitial solute oxygen, but it seemed to be generated by double diffraction. In short, it seemed that the Ti_2O ordered phase did not form despite the presence of a substantial amount of solute oxygen. Judging from the c/a ratio values, the amount of the solute oxygen in the titanium near the titanium-oxygen interface was expected to be comparable to the oxygen content in the Ti_2O phase.

The weak reflection spots near the 1/2 1/2 $\bar{1}$ 1 position in the [1 $\bar{1}$ 0 0] diffraction pattern in Fig. 4b are indicated by the arrow. These spots were not considered to originate from the formation of any ordered structure but indicated an overlap of the TiO phase with the hcp titanium. The TiO phase far from the surface seemed to proceed from a passive state film generated on the specimen in ambient air. Although the passive state film of titanium is considered to be the TiO_2 phase or an amorphous phase, it may be the TiO phase, based on the results of this study. It is also possible that the amorphous passive state film changes to the TiO phase through the electron beam irradiation from the TEM.

In the HRTEM image of Fig. 2c, a contrast modulation corresponding to six times the (0 0 0 2) plane spacing of the hcp titanium can be recognized. The contrast modulation seemed to appear as an interference between the stacks of the (1 1 1) close-packed plane (ABCABC. . .) of the TiO passive film and the (0 0 0 2) close-packed plane (ABABAB. . .) of the hcp titanium.

In the low-magnification image seen in Fig. 1a, some dislocations are evident in the titanium. Generally, dislocations are introduced by a strain due to a difference

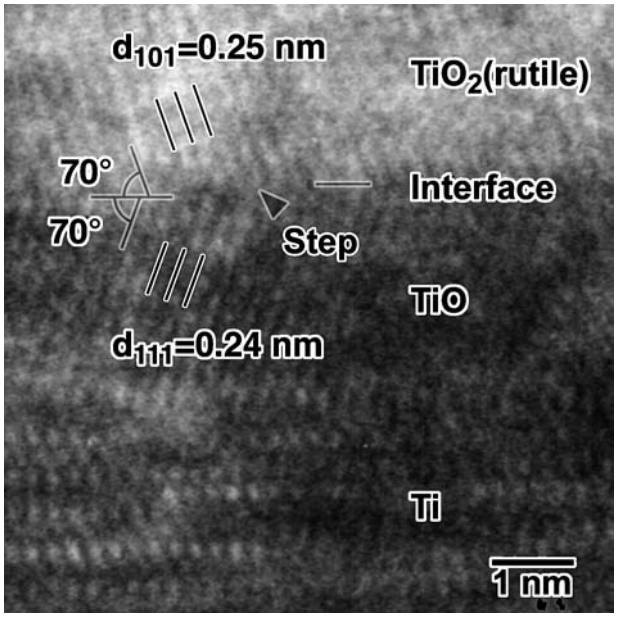

Figure 5 Enlarged HRTEM micrograph of the titanium-TiO-TiO_2 interface. A step is put in at the TiO-TiO_2 interface to maintain partial coherency, as indicated by the arrow.

in the thermal expansion coefficients of the metal and the oxide at the usual PFM junction [4]. Compared to the thermal expansion coefficient values in the titanium ($\alpha \sim 9.4 \times 10^{-6}$ K^{-1}) and the rutile ($\alpha \sim 8.8 \times 10^{-6}$ K^{-1}), the difference is quite small. A strain of 0.05% is estimated for a change in temperature of about 800 K. In contrast, the axial ratio changed approximately 2% due to the change in the solute oxygen content between the interface (Fig. 4a) and the area 5 μm inside the interface (Fig. 4b). In short, the change in the solute oxygen content seemed to cause the formation of the dislocations in the titanium.

The above results show that the hexagonal titanium and the TiO_2 phase of the rutile structure were in contact through the TiO phase that was only a few nm thick at the titanium-surface oxide interface. The transition occurred from the (0 0 0 2) close-packed plane of the hexagonal titanium to the (1 1 1) close-packed plane of the TiO phase. Fig. 5 is a magnified HRTEM image of the interface. The interface of the $(1\ 1\ 1)_{TiO}$ plane and the $(1\ 0\ 1)_{TiO_2}$ plane matched as they tilted toward the interface at the same angle of 70°. Because plane spacing values of d_{111}(TiO) (0.2407 nm [27]) and d_{101}(TiO_2) (0.2487 nm [28]) have been reported, a lattice mismatch between the $(1\ 1\ 1)_{TiO}$ plane and the $(1\ 0\ 1)_{TiO_2}$ plane is anticipated since the tilting angles to the interface are almost the same. To reduce the lattice mismatch, the ideal angle can be estimated as follows. The projections of the $(1\ 1\ 1)_{TiO}$ and $(1\ 0\ 1)_{TiO_2}$ planes on the interface are $d_{111}(\mathrm{TiO})/\sin\theta_1$ and $d_{101}(\mathrm{TiO_2})/\sin\theta_2$, respectively, where θ_1 and θ_2 are inclined angles of the $(1\ 1\ 1)_{TiO}$ and $(1\ 0\ 1)_{TiO_2}$ planes to the interface and given by $\theta_1 = (70 - x)^\circ$ and $\theta_2 = (70 + x)^\circ$, respectively. The continuity between these planes at the interface holds while $d_{111}(\mathrm{TiO})/\sin\theta_1 = d_{101}(\mathrm{TiO_2})/\sin\theta_2$. Then

$$d_{111}(\mathrm{TiO})/d_{101}(\mathrm{TiO_2}) = 0.968 = \sin(70 - x)^\circ / \sin(70 + x)^\circ.$$

And $x = 2.5^\circ$ satisfies this equation. Then the ideal inclined angles to the interface should be 67.5° and 72.5° for the $(1\ 1\ 1)_{TiO}$ plane and the $(1\ 0\ 1)_{TiO_2}$ plane, respectively. As a result, correction of the deviation from the ideal contact angle introduced a step at the TiO-TiO_2 interface, as shown by the arrow in Fig. 5. Consequently, the interface slopes at an average gradient of 2.5° and accommodates itself to the lattice mismatch. However, the lattice coherency of an additional direction on the interface cannot be maintained, even that of one direction can be kept up. Accordingly, the TiO_2 phase near the interface retained its fine crystallite structure due to strong interfacial constraint. Once the TiO_2 crystals left the interface as the surface oxide layer grew, less interfacial constraint permitted these TiO_2 crystals to grow, forming round, granular rutile crystals of about 100 nm (Fig 1b). Finally, the rutile crystal became columnar, since the titanium-oxide interface advanced toward the inside and preferentially grew longitudinally.

3.2. Anodic oxidation

Fig. 6 is an SEM micrograph of the anodized titanium surface. A rough, three-dimensional surface structure with plentiful open pores is characteristic of spark anodization. Generally, an oxide film formed on titanium by the anodization process has high resistivity. If anodization is carried out at a voltage below the breakdown limit, the drop in the voltage will mainly occur over the oxide film. In this case, the final oxide thickness formed by anodization is almost linear, depending on the amount of voltage applied [20]. However, if the voltage exceeds the breakdown limit, the oxide will no longer be resistive enough to obstruct further current flow and oxide growth. Under these circumstances, the anodization process will be accompanied by excessive gas evolution and sparks [20].

Fig. 7 displays a TEM micrograph of a specimen cross section. The lower left corner of the micrograph is the implant surface and the upper right corner is the titanium base. The surface is very rough, and the thickness of the oxide layer is estimated to be about 3–10 μm. A large crack and a pore can be seen between the titanium base and the oxide. A protrusion and depression are found on the surface, the depression being located under the pore. The surface microstructure around the depression is shown in Fig. 8a in a dark field micrograph. The left half displays an amorphous contrast,

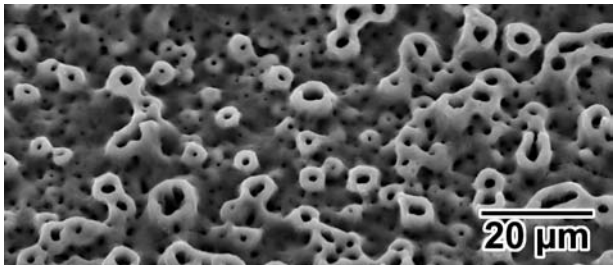

Figure 6 SEM micrograph of the anodized titanium implant surface (TiUnite^{TM}). Extreme surface roughness and a three-dimensional oxide structure consisting of numerous open pores is typical morphology created by spark anodization.

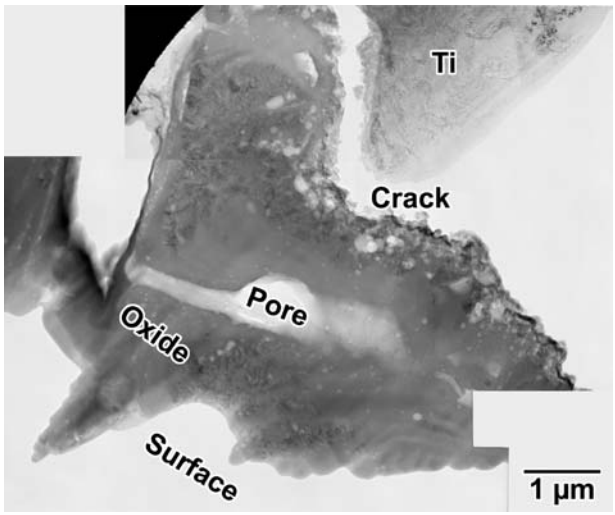

Figure 7 A low-magnification TEM micrograph of the cross section of the anodized titanium surface. The lower portion of the photo is the implant surface and the upper portion is the titanium base.

while the right half is crystalline. The SAD patterns and EDX spectra taken from points "B" through "E" in Fig. 8a are shown in Figs 8b–e. The SAD patterns from the amorphous phase (points "B" and "C") have halos. In contrast, those taken from points "D" and "E" show that the small crystals are a TiO_2 phase of the anatase-type structure. The corresponding area of a selected area aperture is about 100 nm in diameter. Thus, the size of the anatase crystal is estimated to be more than 100 nm. In the EDX spectra measured from the amorphous phase (Fig. 8d and e), a strong phosphorus peak is detected, which is considered to be derived from a phosphate anion; this finding leads to the conclusion that the anodization process must have occurred in a phosphoric solution. The phosphate anion from the electrolyte was incorporated into the oxide layer and concentrated in the amorphous phase.

Fig. 9a shows a low-magnification TEM image of a cross section of the surface. The area in the lower right corresponds to the implant surface where protrusions and a depression are located. In Fig. 7, the anatase phase formed at the depression, while the amorphous phase formed at the depression near the pore in Fig. 9a. There was no correlation between the surface morphology and the phase formed. Fig. 9b and c are SAD patterns taken from positions "B" and "C" in Fig. 9a. Judging from the SAD patterns, the crystal size of the anatase oxide varies from less than 100 nm to less than 10 nm. In particular, nano-crystallites of the anatase phase formed

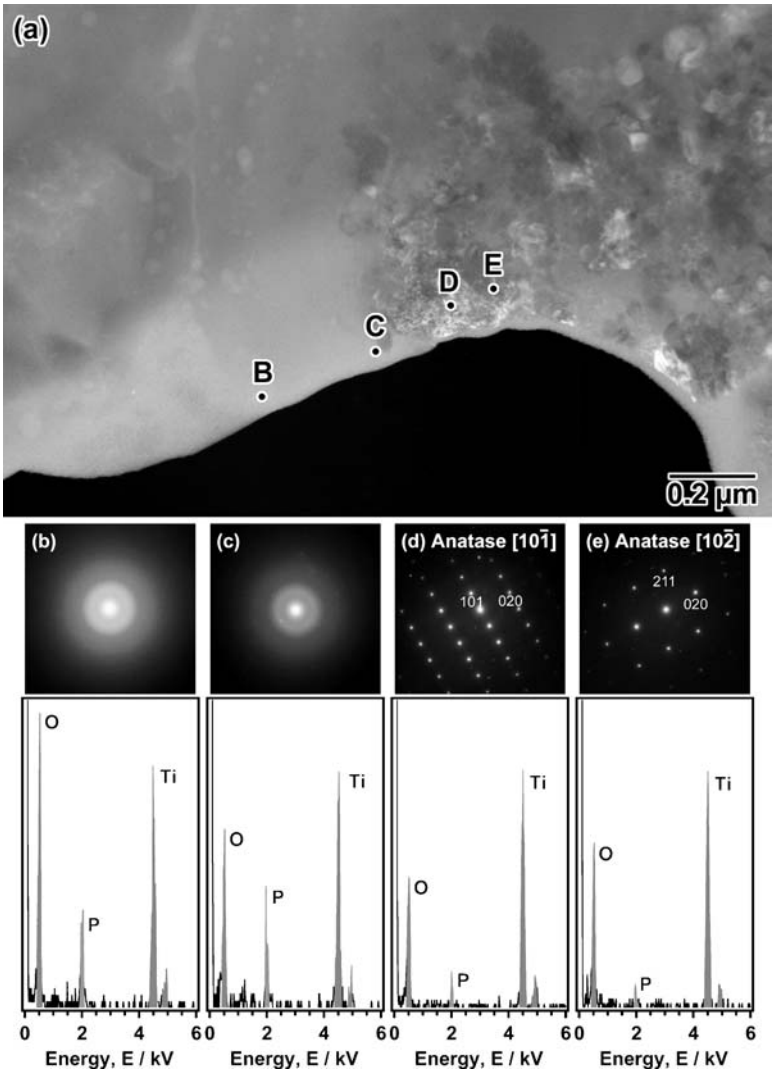

Figure 8 (a) A dark field TEM micrograph of the depression on the surface in Fig. 7. (b–e) Diffraction patterns and EDX spectra measured from points "B", "C", "D" and "E" in Fig. 8a, respectively.

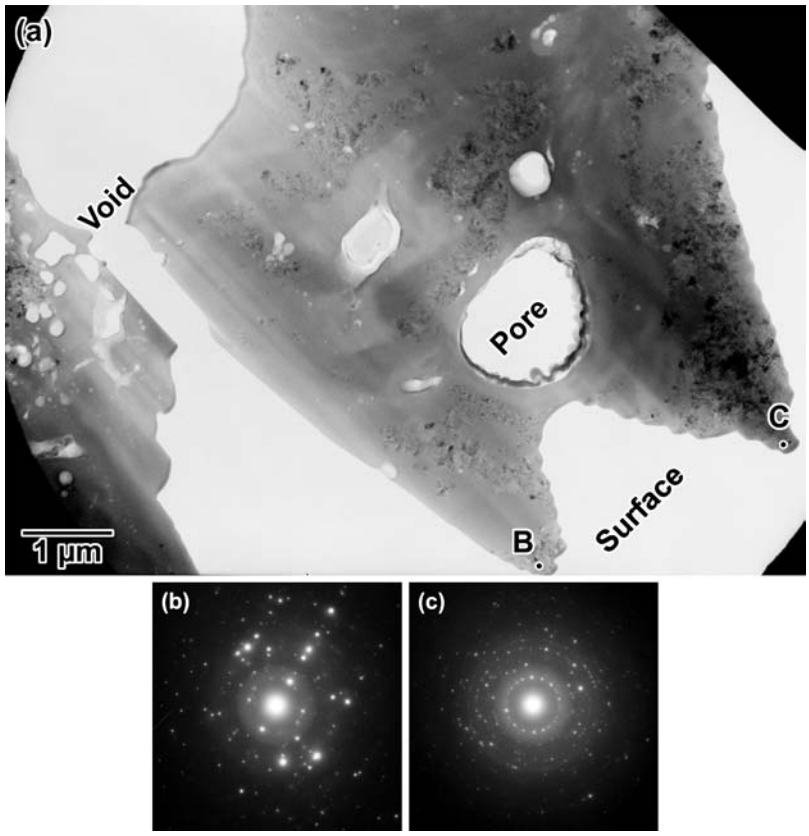

Figure 9 (a) A low-magnification cross-sectional TEM micrograph of the anodized titanium surface. The implant surface is in the lower-right part of the photo, and the titanium base is visible at the left edge. (b, c) Diffraction patterns were taken from the points on the oxide surface marked "B" and "C" in Fig. 9a, respectively.

at position "C" in Fig. 9a. In such a case, enhanced catalytic functions such as photocatalysis, disinfection and hydrophilication are expected [21, 22].

The titanium base is visible at the left side of Fig. 9a. A number of voids were generated to form a zone around the interface between the oxide and the titanium base, as shown in a magnified view in Fig. 10a. Fig 10b is a further magnified image taken near the interface and its corresponding SAD pattern. The hcp titanium, titanium oxide and amorphous phase coincide in an area of about 100 nm, since the SAD pattern indicates an overlap of these three phases. However, there is no clear interface between them, as is the case with the degassed specimens. HRTEM images taken from positions "A" and "B" in Fig. 10b are shown in Fig. 10c and d. Although the crystalline oxide was the anatase-type TiO_2 phase, we seldom found the rutile-type TiO_2 phase, as shown in Fig. 10d. The rutile-type TiO_2 phase did exist in the surface oxide layer, but it was very rare, and usually the crystalline oxide was the anatase-type TiO_2 phase. EDX spectra measured at positions "A"-"C" are displayed in Figs 10e–g. Phosphorus was detected in the amorphous phase (Fig. 10g); the phosphorus content in the amorphous phase around the interface was lower than around the surface. The penetration depth of the phosphoric anion seemed to be related to the phosphorus concentration.

As mentioned above, spark anodization formed a surface oxide layer that was very thick (about 10 μm), and also caused the formation of a huge crack or void around the titanium-oxide interface. Indeed, the crack was detected by examining the scanning ion microscopic image when the TEM specimen was prepared with the FIB. Presumably, the spark anodization process caused such heavy oxidation on the titanium base that the necessity of removing the oxide layer during implantation may need to be considered.

3.3. Comparison between the thermal and anodic oxidations

We investigated the cross-sectional structures of the surface oxide layers for both thermal-oxidized and anodic-oxidized specimens. The conditions for thermal oxidation were a relatively high temperature (1073 K) and reduced atmosphere (27 hPa). The oxide generated was mainly the TiO_2 phase of the rutile structure. The outer structure of the surface oxide layer was composed of columnar crystals of the rutile-type TiO_2 phase. Near the interface, the crystal morphology became round and granular, and the size of the crystals adjacent to the interface was less than 10 nm. The oxide in the surface oxide layer was the rutile-type TiO_2 phase despite the change in morphology of the oxide crystals, depending on their location from the interface to the surface. The morphological change was consistent with the usual crystal growth process.

Between the fine rutile crystallite and hcp titanium at the interface, there was a transitional layer of the TiO phase with a NaCl structure in an almost uniform thickness of a few nm. The close-packed (1 1 1) plane stacking of the TiO phase replaced the close-packed (0 0 0 2) plane stacking of the titanium base. It seemed that coherency between the titanium base

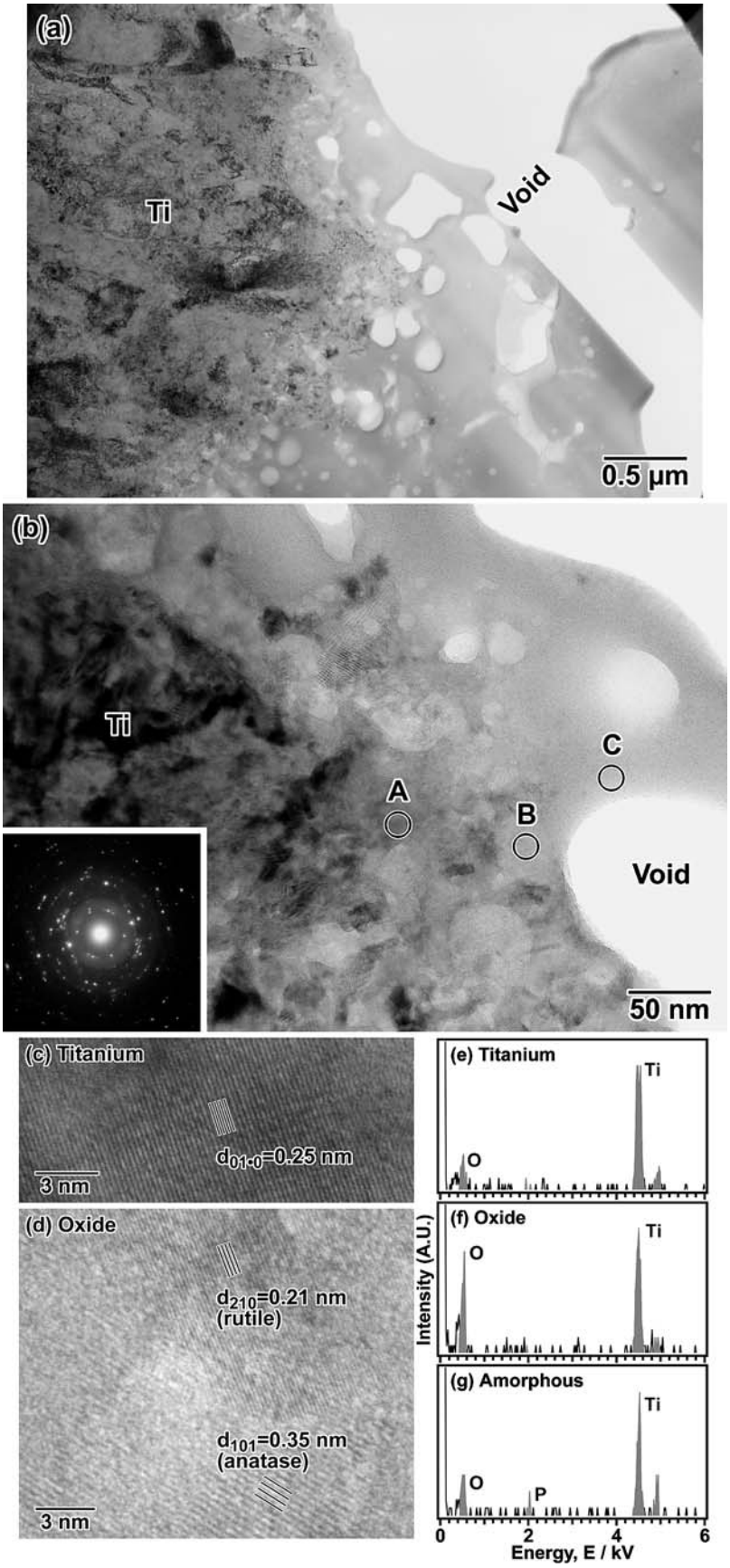

Figure 10 (a) A low-magnification cross-sectional TEM micrograph of the anodized oxide-titanium base interface. Many voids had formed around the interface. (b) An enlarged TEM micrograph and a diffraction pattern (inset) of the interface. The diffraction pattern indicates the overlap of the amorphous, titanium and oxide. (c, d) HRTEM micrographs taken from positions "A" and "B" in Fig. 10b, respectively. (e–g) EDX spectra measured from positions "A", "B" and "C" in Fig. 10b.

and the TiO phase was completely maintained. Partial coherency was retained between the TiO phase and crystallite TiO_2 phase. However, retaining full lattice coherency between the TiO and TiO_2 phases was obviously impossible. The constraint affects the formation of the oxide at the interface, and the crystal size of the oxide is left being fine. In the case of thermal oxidation, a clear interface, composed of the thin transitional layer was observed between the rutile-type oxide and the titanium base.

The conditions of the anodic oxidation, called "spark anodization," were relatively severe. As mentioned above, the thickness of the oxide layer was a maximum of 10 μm, which was composed of a mixture of the anatase-type TiO_2 phase and the amorphous phase in which the phosphoric anion was concentrated. The anatase crystal was relatively small and varied from less than 10 to more than 100 nm. The volume fraction and crystal size may relate to the functions of photocatalysis, disinfection and hydrofilication. The oxide layer formed by the spark anodization was accompanied by a huge crack or void around the interface; defects such as these may lead the surface oxide layer to exfoliate during clinical use. It is suggested that long-term reliability should be examined clinically.

The structures of these two oxide layers, as well as the oxide phases, are quite different. These differences are a natural outcome of the completely different oxidation processes: the thermal oxidation was carried out in a dry environment and the anodic oxidation was performed in a wet environment accompanied by an electrochemical effect.

In this study, we investigated the cross-sectional structures of the surface oxide layers under certain conditions. Changing factors such as the temperature, pressure, and duration of the thermal oxidation and the temperature, voltage, duration, electrolyte, and concentration for the anodic oxidation will cause the compounds and structures formed to vary from those observed in this study. Until now, it was difficult to prepare cross-sectional TEM specimens of metal-oxide composites because of the differences in their mechanical and chemical properties. Nowadays, amazing progress in TEM sample preparation equipment and techniques has made it possible for us to easily observe the interface structure on an atomic scale. Much new knowledge about metal-oxide interface structures will be discovered by atomic-scale TEM observations in the future. We intend to continue to investigate the titanium-oxide interface structure under various oxidation conditions using recent sophisticated techniques like EELS, together with TEM characterization, to optimize the use of biomaterials.

4. Conclusions

We used TEM to investigate the titanium-oxide interface structure formed by the degassing and the anodization processes.

Thermal oxidation occurred in the degassed titanium, and the structure around the surface oxide layer was characterized as follows:

1. The oxide layer was less than 1 μm thick and was composed of the TiO_2 phase with a rutile structure.
2. The shape of the rutile crystals from the surface to the interface varied from columnar to granular to fine.
3. Between the Ti and the rutile, there was a thin intermediate layer a few nm thick. The intermediate layer was considered to be the NaCl-type TiO phase.
4. Lattice coherency was maintained through both of the close-packed planes between the hcp titanium and TiO phase.
5. Partial lattice coherency was observed between the intermediate TiO phase and fine TiO_2 crystallite.

Anodic oxidation on the surface of the titanium implant and the structure of the surface oxide produced the following results:

1. The oxide layer was about 10 μm thick and was composed of a mixture of the amorphous phase and the TiO_2 phase of the anatase structure.
2. The crystal size of the anatase varied from less than 10 nm to more than 100 nm.
3. Phosphorous was concentrated in the amorphous phase.
4. In contrast to the degassed specimens, neither lattice coherency nor a clear interface was found, but a large crack and a void formed around the interface.

Acknowledgements

This study was performed with the help of many coworkers. The degassing treatment and useful discussion on thermal oxidation by Prof. Watanabe at Baylor College of Dentistry are greatly appreciated. Also appreciated was the anodized implant sample provided by Prof. Sawase and Dr. Suketa at Nagasaki University. The author is grateful for permission given by Prof. Kuwano at Kyushu University to use the FIB apparatus. He wishes to thank Prof. Hisatsune, Prof. Shiraishi and Dr. Miura at Nagasaki University for the useful discussions he had with them. Partial financial support for this work was provided by JSPS Grant-in-Aid 13771172 and 15592055.

References

1. R. R. WANG and A. FENTON, *Quintessence Int.* **27** (1996) 401.
2. P. I. BRÅNEMARK, U. BREINE, B. JOHANSSON, P. J. ROYLANCE, H. RÖCKERT and J. M. YOFFEY, *Acta Anat.* **59** (1964) 1.
3. G. F. ANDREASEN and R. E. MORROW, *Ameri. J. Orthodont.* **73** (1978) 142.
4. J.-M. MEYER, in Dentistry, in "Concise Encyclopedia of Medical & Dental Materials", edited by David Williams (Pergamon Press, GB, 1990) p. 307.
5. J. A. PASK, in "Alternatives to Gold Alloys in Dentistry", edited by T. M. Valega (US Department of Health, Education and Welfare Publication No. (NIH) 77-1227. US Government Printing Office, Washington, DC, 1977) p. 235.
6. T. TOGAYA, M. SUZUKI, S. TSUTSUMI and K. IDA, *Dent. Mater. J.* **2** (1983) 210.
7. I.-C. PANG, J. L. GILBERT, J. CHAI and E. P. LAUTENSCHLAGER, *J. Prosthet. Dent.* **73** (1995) 17.
8. L. PROBSTER, U. MAIWALD and H. WEBER, *Euro. J. Oral Sci.* **104** (1996) 313.

9. H. YILMAZ and C. DINCER, *J. Dent.* **27** (1999) 215.
10. M. KÖNÖNEN and J. KIVILAHTI, *J. Dent. Res.* **80** (2001) 848.
11. M. ADACHI, J. R. MACKERT, JR., E. E. PARRY and C. W. FAIRHURST, *J. Dent. Res.* **69** (1990) 1230.
12. M. KÖNÖNEN and J. KIVILAHTI, *J. Biomed. Mater. Res.* **28** (1994) 1027.
13. TORE DÉRAND, *Dent. Mater.* **11** (1995) 93.
14. S. N. WHITE, L. HO, A. A. CAPUTO and E. GOO, *J. Prosthet. Dent.* **75** (1996) 640.
15. N. SUANSUWAN and M. V. SWAIN, *J. Dent.* **31** (2003) 509.
16. H. GARBACZ and M. LEWANDOWSKA, *Mater. Chem. Phys.* **81** (2003) 542 .
17. T. HANAWA, M. KON, S. OHKAWA and K. ASAOKA, *Dent. Mater. J.* **13** (1994) 164.
18. J. A. HAUTANIEMI, H. HERØ and J. T. JUHANOJA, *J. Mater. Sci.: Mater. Med.* **3** (1992) 186.
19. M. B. LUPESCU, M. ZAHARESCU and A. ANDREI, *Mater. Sci. Engineer.* **A232** (1997) 73.
20. JUKKA LAUSMAA, in "Titanium in Medicine," edited by D.M. Brunette, P. Tengvall, M. Textor and P. Thomsen (Springer, Berlin, 2001), p. 231.
21. A. FUJISHIMA and K. HONDA, *Nature* **238** (1972) 37.
22. R. WANG, K. HASHIMOTO, A. FUJISHIMA, M. CHIKUNI, E. KOJIMA, A. KITAMURA, M. SHIMOHIGASHI and T. WATANABE, *ibid.* **388** (1997) 431.
23. J. B. LAI, L. J. CHEN and C. S. LIU, *Micron* **30** (2000) 205.
24. J. BONEVICH, D. VAN HEERDEN and D. JOSELL, *J. Mater. Res.* **14** (1999) 1977.
25. S. ANDERSSON, B. COLLÉN, G. KRUUSE, U. KUYLENSTIERNA, A. MAGNÉLI, H. PESTMALIS and S. ÅSBRINK, *Act Chem. Scandin.* **11** (1957) 1653.
26. ICDD crad: 44-1294.
27. ICDD card: 8-117.
28. ICDD card: 21-1276.

Received 29 July 2004
and accepted 31 January 2005